

Modeling and optimization of dry reforming of methane over Ni-Co/Al₂O₃-ZrO₂ catalyst coating via PVD method in a microchannel reactor using Box-Behnken design

Mohamadgafar moradi

Islamic Azad University

Gholamreza Moradi (✉ gmoradi@razi.ac.ir)

Razi University

Amir Heydarinasab

Islamic Azad University

Alimorad Rashidi

Research Institute of Petroleum Industry (RIPI)

Research Article

Keywords: Dry reforming of methane, microchannel reactor, thermal evaporation deposition, Ni-Co/Al₂O₃-ZrO₂ thin films, response surface method

Posted Date: April 21st, 2022

DOI: <https://doi.org/10.21203/rs.3.rs-1504542/v1>

License:  This work is licensed under a Creative Commons Attribution 4.0 International License. [Read Full License](#)

Abstract

In the current study, to optimize dry reforming of methane, coating Ni-Co /Al₂O₃-ZrO₂ nanocatalyst was explored in a microchannel reactor using physical vapor deposition (PVD) method. The Box-Behnken design was implemented to examine initial feed conversion (CO₂, CH₄), H₂:CO molar ratio and catalyst deactivation. Using response surface method, optimization of coating time (2 min, 3 min, and 4 min), Co/Ni weight percentage (25%, 50%, and 75%), and reaction temperature (650 °C, 700 °C, 750 °C) was explored. The experiments were conducted when the temperature ranged from 650 °C to 750 °C, the pressure was equal to 1 atm, and CH₄/CO₂ molar ratio was equal to 1. Also, Grazing incidence X-ray diffraction (GIXRD), field emission scanning electron microscopy (FESEM), and energy-dispersive X-ray (EDX), were used to identify catalyst features. FESEM images showed that catalyst film activity highly depended on coating time in that increasing coating time yielded more uniform and properly dispersed catalyst particles. When deposition time was 4 min, nearly 95% of the particles had a size of 10-20 nm (with an average of 15.41 nm). EDX analysis also indicated that all elements were uniformly and properly dispersed on the substrate. GIXRD analysis further demonstrated that increasing Co/Ni weight percentage up to 50% would result in reduced particle size as well as higher activity, stability, and resistance to carbon deposition. Conversely, greater Co weight percentages led to relatively larger particle size and lower catalytic activity given that the active sites were synthesized and the Ni particles were covered by the Co-rich phase. Concerning the optimum condition, the highest amounts of initial CH₄ conversion (95.94%), initial CO₂ conversion (97.87%), H₂:CO molar ratio (0.96), and catalyst deactivation (1.99%) were registered when the coating time was 3.87 min, Co/Ni weight percentage was 45.04%, and the reaction temperature was 750 °C. The values predicted in the proposed model closely aligned with the results obtained through experimental tests.

1. Introduction

Producing synthesis gas from greenhouse gases has become an interesting and challenging subject in the face of issues like global warming and its undesirable consequences [1]. Dry reforming of methane (DRM) is the main process of producing synthesis gas with a molar ratio of one. An advantage of using this method is the high purity of the generated CO [2]. The synthesis gas prepared through DRM can be used in producing methanol and dimethyl ether (C₂H₆O) as well as in Fischer-Tropsch process and carboxylation [3]. Carbon deposition is the major problem in the DRM process. The two reactants in this process – namely CO₂ and methane (CH₄) – contain carbon, which is deposited as a result of the reaction leading to catalyst deactivation [4–5]. To date, numerous studies have explored the performance of noble and non-noble metals in DRM. The results suggest that although noble metals are highly resistant to carbon deposition, their large scale use is not economical due to their high expenses. On the other hand, non-noble metals like Nickel (Ni) demonstrate enhanced and more economical catalytic activity at the expense of higher carbon deposition [6–7]. Due to methane decomposition and the Boudouard reaction in DRM, such catalysts are more susceptible to coke formation, hence reducing catalyst stability to some extent [8–10]. Since using support in the DRM process plays a critical role in boosting catalytic activity and minimizing carbon deposition, Gamma-alumina (γ-Al₂O₃) is utilized in many cases as the support for nickel-based catalysts [11, 12, 13]. Various studies have investigated ways to improve the performance and stability of Ni/Al₂O₃ as well as its resistance to coke formation, with the findings indicating the effectiveness of adding promoters [14, 15, 16]. Among different promoters used for nickel-based catalysts, zirconium dioxide (ZrO₂) and cobalt (Co) have received special attention [17–19]. Adding an appropriate amount of Co results in strong metal-support interaction, reduces particle size, and improves resistance to coke formation, thus enhancing

catalytic activity [20–21]. Research has displayed that using a combination of Ni and Co as the catalyst, with the proportion of the latter ranging from 3–5%, yields acceptable performance [16]. On the other hand, given its good oxidation-reduction and oxygen mobility properties, ZrO_2 increases the dispersion of carbon and facilitates its gasification, hence preventing carbon deposition. Moreover, ZrO_2 hinders the entrance of the active phase into alumina structure and active spinel phase development ($NiAl_2O_4$) [22–23]. This promoter is also recognized as an acid-base bi-functional catalyst since CO_2 is an acid gas and requires a base site to be adsorbed on the catalyst surface. Therefore, ZrO_2 can function as a base catalyst in DRM, increasing CO_2 adsorption [23]. It has been demonstrated that using a 10% weight ratio of ZrO_2 in the support can yield catalyst's optimum performance in DRM [24]. Sharifi et al. [25] explored the impact of sol-gel method and the inclusion of Co and copper (Cu) promoters on the performance of Ni/ Al_2O_3 - ZrO_2 catalyst in a fixed bed reactor. The results showed that adding promoters, especially Co, to Ni/ Al_2O_3 - ZrO_2 nanocatalyst led to particle size reduction and uniformity in nanocatalyst dispersion. It was also found that adding Co would improve feed conversion, product efficiency, and the ratio of synthesized gas. The researchers discovered that, during the 1440-minute test, Ni/ Al_2O_3 - ZrO_2 synthesized by the sol-gel method had the highest performance when the temperature was 850°C. Since in the fixed-bed reactors the catalytic particles have various sizes and are randomly dispersed on the bed, the reactants register uneven access to the catalyst surface. This leads to the formation of uneven flow patterns and the formation of hot spots and high thermal gradients in exothermic reactions, hence significantly undermining the reactor's performance. To eliminate the problems associated with fixed-bed reactors, structured reactors have been introduced as valuable alternatives in different processes [26]. Microchannel reactors constitute one specific type of structured reactors. One of the major features of microchannel reactors is their high surface area to volume ratio. Thus, they are expected to be highly efficient in terms of thermal performance. The main advantage of this phenomenon is the rise of operating temperature and reaction conversion. In other words, exploiting reactors that are smaller in volume and require lower amounts of catalyst does not make any change in the amount of conversion. Yet, their smaller size results in less energy consumption and lower operating costs [27]. In another study, Kim et al. [28] designed a microreactor system and explored its efficiency and stability in partial oxidation of DME for hydrogen production. Its performance was then compared with that of a conventional pack bed reactor. The microchannel reactor had a thin layer of Al_2O_3 as catalyst support on the surface of the microreactor, while, in the fixed-bed reactor, Al_2O_3 balls were densely packed in a quartz tube. Using enough amounts of catalyst (0.5% wt Ru), both reactors demonstrated similar degrees of conversion. Declining the amount of Ru, however, resulted in reduced efficiency in the conventional fixed-bed reactor, whereas the efficiency of the microchannel reactor remained intact. Sangsong et al. [29] synthesized two Ni-based catalysts – namely 10 wt.% Ni/MgO and 10 wt.% Ni/ Al_2O_3 -MgO – using sol-gel method. Both catalysts were applied in DRM as catalyst pellets and catalyst-coated plates. The results showed significant decline in carbon deposition when the catalyst was coated as a thin film on the microreactor plate. Mahmoudizadeh et al. [30] explored the performance of methanol steam reforming in a microchannel and a fixed-bed reactor, with the findings displaying significantly higher amounts of methanol conversion in the microchannel reactor. The researchers attributed this to the reactants' better access to the active sites. Concentrating on the amount of catalyst coating, Bawornruttanaboonya et al. [31] compared autothermal biogas reforming over a Re-Ni/ Al_2O_3 catalyst in a split-and-recombine microreactor with that of a conventional reactor. In particular, they examined the influence of various inlet feeds and temperatures in an attempt to figure out the optimum condition. In all cases, the highest amount of CH_4 and CO_2 conversion, the lowest concentration of H_2O , and the lowest degree of hot spot formation were registered in the split-and-recombine microreactor. Rezaei et al. [32] investigated the performance of DRM in a researcher-designed microchannel reactor using an

Ni/Al₂O₃ catalyst coated on a stainless steel plate via sputtering method. Since in a microchannel structure a thin film of the catalyst covers the metal surface, the reactor shows a much lower pressure drop in comparison with the time a fixed-bed reactor is used [27]. In general, irrespective of the method used for catalyst coating, the catalyst features (e.g., crystallite phases, morphology, and active phase dispersion) must be retained. Additionally, the selected method should provide uniform coating, desirable catalyst loading, and suitable adhesion [33]. Physical vapor deposition (PVD) is a novel method for coating various materials. Using this method, thin films can be physically coated over the substrates. Coatings produced through PVD can also be utilized with different metallic parts at various temperatures. PVD can assist in creating durable and high quality uniform coatings which are economical as well [34]. The current study was an initial attempt to examine the optimum performance of an Ni-Co/Al₂O₃-ZrO₂ catalyst in a microchannel reactor using PVD for catalyst coating. To this end, the Box-Behnken design (BBD) was adopted to study the impact of various parameters (i.e., coating time, Co/Ni weight percentage, and reaction temperature at three levels) on initial feed conversion, CO₂ and CH₄, H₂:CO molar ratio, and catalyst stability with the aim of identifying the optimum condition.

2. Materials And Methods

2.1. Microchannel reactor

The microchannel reactor used in this study was designed as a flat plate made from an SUS4841 stainless steel sheet. In order to minimize pressure drop and increase efficiency through raising contact time in both inner sides of the microreactor, 26 microchannels, with a width of 1 mm, a depth of 0.5 mm, were machined via a splitting-jointing flow (SJF) in an alternative manner using the computer numerical control (CNC) technology. In order to have a more uniformly distributed flow, the feed was first directed through a triangular manifold in the microchannel reactor inlet. Moreover, to facilitate catalyst replacement after the process, a 4841 stainless steel sheet with a thickness of 1 mm and the size of 48 × 20 mm² was utilized. The sheet was coated by catalyst thin films on both sides and was inserted between the two covering plates of the microreactor. To avoid gas leakage at high temperatures, the developed structure was sealed by a 1 mm thick full face graphite gasket and a 0.5 mm thick internal cuprous gasket. The two covering plates of the reactor were sealed using stainless steel nuts and bolts. Figure 1 displays design details.

2.2. Catalyst coating system

Electron beam evaporation method, which is a type of Physical vapor deposition (PVD) in vacuum, was used to coat the stainless-steel substrates. The main steps of this method include evaporation of source material, vapor transfer from the source material to the substrate, and formation of a thin film over the substrate through vapor deposition. The benefits of this method are the researchers' ability to have control over film thickness and the amount of material deposition. In this method, the required energy for the evaporation of the source material (i.e., the material used as the substrate coating) is provided through transferring electrons' energy to the source material. One of the problems in this method is the likelihood of the oxidation of evaporated metals. In other words, if the system contains oxygen, it may react with the evaporated metal. Furthermore, the presence of oxygen molecules during the metallic vapor transfer from the source material to the substrate leads to reduced deposition rate and hinders coating formation with high density. It is therefore essential to create a vacuum environment to reduce the likelihood of the interaction between molecules and prevent metallic vapor oxidation. This vacuum was attained via using a combination of mechanical and turbo pumps. In the process of vapor deposition using

electron beams, a beam of high energy electrons is sent from the filament to the source material, providing the necessary energy for the evaporation of the source material. Electron beam evaporation comprises a system with an anode and a cathode. Through applying a direct voltage of 10–40 kV, the electrons leave the filament and move toward the source material. The filament is usually made of tungsten. In fact, tungsten-based filaments are the most widely used type of filament in the electron beam evaporation method because of its very high melting point (3422°C). Raising the temperature of the tungsten-based filament provides the energy required for electron beam movement. All the generated electron beam does not move directly toward the source material. Indeed, the electron beam is focused and accelerated using cylindrical lenses. It is also bent by the use of a magnetic field.

As the high energy electron beam strikes the source material and heats it, the source material begins to evaporate releasing high amounts of vapor. The movement of the released vapor from the material to the substrate is stimulated by the pressure difference. When the vapor released from the source material reaches the substrate, it is condensed and transfers its heat to the substrate changing from the vapor phase to the solid phase. It is worth noting that if the optimum design condition (e.g., the distance between the source material and the substrate) is not met, it is likely that the substrate is melt by the vapor. In fact, the large distance between the source material and the substrate results in the condensation of vapor before it reaches the substrate. In contrast, very short distance between the source material and the substrate may lead to the latter's meltdown as it comes to contact with the vapor. The cathodes used in the electron beam method are typically made of copper or graphite because of their appropriate heat transfer. Thus, the cathodes' temperature can easily decrease through water cooling. It is important to make sure that the cathodes react with the source material. The electron beam contains a huge number of electrons. When it is exposed to the source material, the part of the material surface which is in contact with the beam is charged preventing the movement of electrons to other parts. Consequently, the cathode should be connected to earth for the transfer of extra electrons. It should be noted that the electron beam is not focused on one point of the source material only; rather, it is swept across the entire surface. In fact, if the electron beam is focused on a particular point of the source material, it is perforated due to the electron beam's high level of energy. On the other hand, some oxides, like Al_2O_3 , are decomposed into AL, Al_2O , and AlO_3 , causing differences between the source material and the precipitated coating in terms of stoichiometric ratio and chemical composition. A viable procedure to produce oxide coatings that are decomposed as a result of exposure to electron beam is injecting oxygen into the chamber. Since the metal inside the cathode evaporates as it comes into contact with the electron beam, the metallic vapor reacts with oxygen in the presence of the substrate forming a layer of metallic oxide on the surface. The material that evaporates as a result of exposure to the electron beam moves toward the substrate in a straight line. In order to form coatings with uniform thickness, the substrates are placed on spinners and rotate during the process. In addition, some protection plates are placed inside the chamber to prevent the dispersion of the vapor as it moves from the source to the substrate. These protection plates block vapor dispersion inside the chamber, which results in the contamination of other machine parts. They also enhance the process efficiency as their presence facilitates the precipitation of the entire vapor over the substrate. The coating obtained through electron beam evaporation is applied on the substrate through the germination and growth process. Gas atoms and molecules that are separated from the source material and reach the substrate with high temperature transfer their heat energy to the substrate and move over it. Their heat energy is eventually lost and they are adhered to the substrate forming a set of atomic nuclei over it. As this process continues and the number of nuclei on the substrate goes up, the nuclei stick to each other covering the surface of the substrate in the form of a thin film. In this study, the coating process was accomplished in two stages. At first, we aimed to increase surface roughness to improve the catalyst film absorption. To this end, both sides of the stainless steel substrates underwent uniform sanding. Stage one (catalyst support): Since the same substrate was used for all the plates

and Al₂O₃ catalyst promoted by ZrO₂ (with a weight ratio of 10%) was used as the support, all the plates were coated under the same operating conditions and evaporation time. In light of the support features and after several rounds of experiment, it was concluded that 8 minutes would be the optimum evaporation time. In order to deposit thin films of Al₂O₃ on a stainless steel substrate, a 99.99% pure aluminum target (diameter = 100 mm and thickness = 3 mm) and ZrO₂ granules with a density of 5.68 g/cm³ inside the tungsten cathode were used through adopting the high temperature vacuum evaporation method. In this process, the support was coated using argon with 10% oxygen. At first, the initial pressure inside the chamber was set at 5 × 10⁻⁵ mbar. Then, argon and oxygen were fed into the chamber with a $\frac{P_{O_2}}{P_{Ar} + P_{O_2}}$ ratio of 10%, rising the pressure to 0.2 mbar. The evaporation process was performed at room temperature and the catalyst films were deposited in 8 minutes. Stage two (coating Ni promoted by Co): Upon coating the thin films of Al₂O₃ promoted by ZrO₂, the Ni was coated using a 99.99% pure Nickel target (diameter = 100 mm and thickness = 3 mm). To optimize the amount of catalyst and explore its impact on the process, three Co/Ni weight percentages (i.e. 75%, 50%, and 25%) were used. To identify the amount of Co sputtered on the Ni target, a number of 99.99% pure Co chips (3 × 5 mm²) were utilized. Sputtering was performed in 2, 3, and 4 minutes in light of the evaporation time. Argon was used to sputter the Co-promoted Ni. The evaporation process was performed at room temperature and the catalytic films were coated in 2, 3, and 4 minutes.

2.3. Experimental setup for catalytic performance test

DRM in the microchannel reactor, three variables – namely deposition time (t), Co/Ni weight percentage, and reaction temperature (T) – were hypothesized to influence initial feed conversion, H₂: CO molar ratio, and catalyst deactivation. The procedure applied for calculating the percentage of initial feed conversion, catalyst deactivation, H₂: CO molar ratio, and carbon balance is presented below.

$$X_{CH_4} \% = \frac{C_{CH_4 in} - C_{CH_4 out}}{C_{CH_4 in}} \times 100 \quad (1)$$

$$X_{CO_2} \% = \frac{C_{CO_2 in} - C_{CO_2 out}}{C_{CO_2 in}} \times 100 \quad (2)$$

$$Deactivation(\%) = \frac{initial X_{CH_4} - final X_{CH_4}}{initial X_{CH_4}} \times 100 \quad (3)$$

$$\frac{H_2}{CO} = \frac{C_{H_2 out}}{C_{CO out}} \quad (4)$$

$$C_{Balance} = \frac{C_{CO_2 out} + C_{CH_4 out} + C_{CO out}}{C_{CH_4 in} + C_{CO_2 in}} \times 100 \quad (5)$$

2.4. Box-Behnken design

Box-Behnken design (BBD) was applied in this study. To this end, the three variables of coating time, Co/Ni weight percentage, and reaction temperature were regarded as independent variables influencing initial CH₄ conversion, catalyst deactivation, and H₂:CO molar ratio.

Table 1 demonstrates the test variables and their three levels following BBD. High, moderate, and low levels are respectively represented by -1, 0, +1. The test design was identified through selecting the reaction variables and

determining the high and low levels for each of them (see Table 2).

Table (1): Reaction variables and their levels in BBD

Variables	Unit	Symbol	Levels		
			-1	0	+1
Deposition time	min	t	2	3	4
Co/Ni weight percentage	%	X	25	50	75
Reaction temperature	°C	T	650	700	750

Design Expert 7 was used to conduct modeling, analyze model fit indices, obtain coefficients of the fitted model, and identify the optimum condition. Additionally, the experimental tests were carried out in accordance with BBD to estimate the impact of different independent variables (Table 2). Further, response surface methodology (RSM), which is an appropriate alternative in optimization, was exploited to obtain the optimum condition. RSM yields a mathematical model comprising the estimation of linear and nonlinear changes, the interactions among variables, and the significance of each parameter based on the obtained coefficients (Eq. 6). RSM is capable of estimating the absolute error through replicating the central point, based on which the interaction among all variables is assessed.

$$y = \beta_0 + \sum \beta_i x_i + \sum \beta_{ii} x_i^2 + \sum \sum \beta_{ij} x_i x_j \quad (6)$$

Table (2): Test design for the three independent variables and responses

Number	t(S)	X(%)	T(°C)	X _{CH4}	X _{CO2}	H ₂ /CO	Deactivation%
1	750	5	2	90	93	0.89	1.6
2	700	5	3	77	80	0.78	3.9
3	650	2.5	3	46	57	0.46	6.9
4	700	5	3	80	85	0.77	3.6
5	750	5	4	92	97	0.96	2.7
6	700	2.5	2	49	62	0.52	6.4
7	650	7.5	3	36	40	0.53	8.9
8	750	2.5	3	84	86	0.91	2.9
9	650	5	2	31	36	0.64	6.5
10	700	7.5	2	43	53	0.61	7.1
11	700	7.5	4	68	75	0.79	5.8
12	650	5	4	73	76	0.68	4.6
13	750	7.5	3	80	88	0.83	4.3
14	700	5	3	78	82	0.75	3.7
15	700	2.5	4	87	91	0.86	4.1

3. Results And Discussion

3.1. Features of the sputtered catalyst

3.1.1. GIXRD

Figure 3 displays the GIXRD pattern of the Ni-Co/Al₂O₃-ZrO₂ thin films under the following testing condition: deposition time: 4 min; Co/Ni weight percentages: 25%, 50%, and 75%; and scanning range: 2θ=10-80. GIXRD patterns demonstrate some peaks at 2θ = 37.4, 42.8, and 45.8°, which are related to Al₂O₃ (JCPDS 00-004-0880) thin films. Moreover, thin films of ZrO₂ (JCPDS 00-013-0307) are observed at 2θ = 17.9 and 50.7°. Some peaks are also observed at 2θ =37.3,43.4,and 75.6°, which may be related to the cubic phase of NiO (JCPDS 00-004-0880).Considering the peaks identified for NiO, the one at 2θ= 43.4° is regarded as the main peak. Finally some peaks are also identified at 2θ = 19.8, 37.2, 45, and 65.3°, which are attributed to the cubic phase structure of Co₃O₄ (JCPDS 01-076-1802). The absence of any identifiable peak in NiAl₂O₄ and CoAl₂O₄ spinel compounds may be connected to the proper dispersion of phases, especially ZrO₂, which blocks the impregnation of Co and Ni onto the alumina structure. Previous findings also support the idea that the presence of ZrO₂ prevents the growth of crystallite phases and spinal compound production [11-12]. It is observed that increasing the Co/Ni weight percentage up to 50% led to lower peak intensity and smaller particle size. In the Co/Ni weight percentage of 50%, since dispersion goes up and particle size dwindles, amorphization takes place in the studied phases and peaks become less intense and wider. (Figure 3-b). This situation is more clearly observed for ZrO₂ given that no proper

peak is observed in Figure 5-b. Therefore, peaks with the lowest intensity are observed in samples with 50% Co/Ni weights. It is observed that NiO peak intensity rose when Co/Ni weight percentage exceeded 50% (Figure 3-c). Increasing the Co weight percentage from 50% to 75% resulted in the decline of FWHM from 0.7360 to 0.5697 and rise of crystallinity. Based on calculations in light of Debye-Scherrer ($0.9 \lambda/W \cos \theta$), in Co/Ni weight percentages of 25%, 50%, and 75%, the particle sizes of catalytic films were found to be 18.49, 11.65, and 15 nm respectively. This shows that the particle size of catalytic films decreased when the Co weight percentage went up to 50%. Larger particle size in the Co/Ni weight percentage of 75% may be attributed to the interactions between neighboring Co-Co ions or the substitution of a large number of Co^{+2} ions (72 Å) with Ni^{+2} ions (69 Å) in the NiO lattice. This phenomenon degrades the crystallinity of NiO films and drops the amount of NiO in NiO-Co composite films.

3.1.2. FESEM analysis

Figure 4 demonstrates FESEM images for 2 min, 3 min, and 4 min deposition times on scale of 200 nm. The findings suggest that surface morphology changes as a result of variation in deposition time. In particular, increasing the deposition time leads to smaller particle size and more uniform dispersion. In fact, the sample undergoing 4 min deposition contains denser and more uniform particles in comparison with the samples being exposed to 2 and 3 min deposition time. Thus, in the sample undergoing 4 min deposition, the coating has properly covered the substrate, suggesting that raising deposition time improves the distribution of particle size, catalyst loading, and structure uniformity. It is clearly observed that, for the sample with a deposition time of 4 min, the sputtered film looks like a cauliflower, which is a common surface morphology for metallic coatings prepared through this method [35, 36, 37]. Closer inspection indicates that raising deposition time reduces surface roughness and enhances particle density. Additionally The results of statistical analyses related to particle size distribution are presented in Fig. 4 (a, b, and c). These results suggest that, in the sample undergoing 4 min deposition, the average particle size was 15.41 nm, with the smallest and biggest particles registering sizes of 11.02 nm and 22.38 nm respectively. Considering the sample catalyst exposed to 3 min deposition, the average particle size was 53.32 nm, with the particle sizes ranging from 21.375 nm to 94.695 nm. The average particle size in the sample undergoing 2 min deposition was found to be bigger than that undergoing 3 min deposition. More precisely, the average size for the former sample was 71.46 nm, with the maximum and minimum particle sizes respectively being 131.72 nm and 34.45 nm. The results of data analysis demonstrate that increasing deposition time led to smaller particle size. Indeed, all sputtered particles in the 4 min deposition time were smaller than 25 nm, while around 10% of the particles in the sample exposed to 2 min deposition were bigger than 100 nm, which could be appropriate spots for carbon deposition leading to catalyst deactivation.

3.1.3. EDX dot-mapping analysis

Table 3 illustrates the EDX analysis of Ni-Co/ Al_2O_3 - ZrO_2 catalyst coatings at 4 min deposition time and Co/Ni weight percentages of 50%. It is observed that the catalysts were dispersed over the supporter with acceptable weight percentages, indicating the high accuracy of the coating process in the present study.

Table (3): EDX dot-mapping analysis for the Co/Ni weight percentages of 50% and 4 min deposition time

Let	Line	Int	Error	K	Kr	W%	A%
O	Ka	85.5	8.7996	0.2934	0.1371	20.13	24.81
Al	Ka	96.6	8.7996	0.4976	0.3174	57.82	55.72
Co	La	8.7	0.3227	0.0434	0.0408	4.98	9.78
Ni	La	34.1	8.7996	0.1005	0.0911	10.03	5.01
Zr	La	10.3	0.3227	0.0651	0.0515	7.04	4.68
Sum				1	0.6379	100	100

Additionally, All elements used in the physical vapor deposition process are observable in Fig. 5 the images of EDX spectra for Ni-Co/Al₂O₃-ZrO₂ catalyst coatings at the deposition time of 4 min and Co/Ni weight percentage of 50% indicate that all elements are uniformly dispersed on the substrate.

3.2. Catalyst performance in DRM

3.2.1. Data analysis

Normal distribution of the residuals is a basic assumption in the analysis of variance (ANOVA). If this assumption is violated, the results of ANOVA and the obtained model will not be valid. The main approach to test this assumption is checking the normal probability plot of studentized residuals, which is illustrated in Fig. 6a-d. It is obtained through dividing the residual at each point by its corresponding variance. The data are believed to be normally distributed if the residual points are suitably located around a straight line. The following figures display the normal probability plots for the current study. As observed, the data points have formed a relatively straight line and nonlinear pattern is not detected. Therefore, the assumption of normality of residual distribution is met.

3.2.2. Model fit indices

The fitness of a model is identified through considering the F-value and its corresponding p-value. Bigger F-values and smaller p-values indicate better models. In the current study, the confidence interval was set at 95%, meaning that p-values smaller than 5% would indicate significant models [38]. Table 4 presents a summary of the statistical analyses carried out to test model fitness. Model fitness was assessed in light of standard deviation and PRESS (the lower, the better) as well as coefficient of determination (R^2), adjusted coefficient of determination (R^2 adj.), coefficient of prediction (R^2 pred.). For the last three indices, higher values demonstrate better model fitness. The second order model was considered fit for the initial feed conversion and catalyst deactivation, while the first order model was selected for H₂/CO molar ratio. Smaller PRESS values indicate lower sum of squared residuals in predicting responses, hence higher accuracy of the model in predicting responses (R^2 pred.). Also, the negligible difference between R^2 and R^2 adj. in the proposed models shows that the insignificant sentences were removed in these models. The coefficient of determination (R^2) is also close to 1, indicating the strong correlation between the experimental results and the proposed model.

Table (4): Model summary statistics

	initial CH ₄ conversion	initial CO ₂ conversion	deactivation	H2:CO ratio
std. dev.	3.66	2.51	0.56	0.082
R-squared	0.9889	0.994	0.9719	0.7761
adj.R-squared	0.9689	0.9831	0.9213	0.715
pred.R-squared	0.8331	0.9370	0.562	0.5328
adeq.precision	22.347	30.537	14.981	11.319

3.2.3. Exploring the significance of second order model fit indices for initial CH₄ conversion

Since the p-value is smaller than 5%, second order model fit is approved for describing changes in the initial CH₄ conversion. On the other hand, given that the p-value was greater than 5% for C², A², BC, and AB sentences, these sentences are not significant in the second order model. The effect size for the impact of the independent variables on initial CH₄ conversion can be assessed in light of the F-values. According to the F-values displayed in Table 5, reaction temperature (T) exercised the highest influence on initial CH₄ conversion. In contrast, the lowest impact was registered for Co/Ni weight percentage. The coefficient of determination (R²) is 0.9889, demonstrating the model accuracy in predicting responses. The model's fitness accuracy is 22.347, showing that this model can be suitably used to assess initial CH₄ changes in the entire experiment.

Table (5): ANOVA results for the second order response model for initial CH₄ conversion

Source	Sum of squares	Mean Square	F Value	p-value Prob > F	Coefficient Estimate	Standard Error
Model	5964.68	662.74	49.52	0.0002		
A-t	1431.13	1431.13	106.93	0.0001	13.38	1.29
B-X	190.13	190.13	14.21	0.0130	-4.88	1.29
C-T	3200.00	3200.00	239.10	< 0.0001	20.00	1.29
AB	42.25	42.25	3.16	0.1358	-3.25	1.83
AC	400.00	400.00	29.89	0.0028	-10.00	1.83
BC	9.00	9.00	0.67	0.4495	1.50	1.83
A ²	40.01	40.01	2.99	0.1444	-3.29	1.9
B ²	652.31	652.31	48.74	0.0009	-13.29	1.9
C ²	46.31	46.31	3.46	0.1219	-3.54	1.9

Finally, the following equations represent the second order model fit indices for initial CH₄ conversion in light of the coded values of independent variables. Higher coefficients of a sentence in the coded model indicate the bigger influence of that variable on initial CH₄ conversion. Moreover, considering the coefficient signs, positive sign indicates direct relationship, whereas negative sign demonstrates inverse relation between these coefficients and initial CH₄ conversion.

The model based on coded values of the independent variables:

$$XCH_4 = +78.33 + 13.38A - 4.88B + 20.00C - 3.25AB - 10AC + 1.5BC - 3.29A^2 - 13.29B^2 - 3.54C^2 \quad (7)$$

The model based on the actual values of the independent variables:

$$XCH_4 = -1406.50000 + 1.481667X + 179.62500t + 2.92333T - 0.130000x^2 + 1.20000E-003xT - 0.20000t^2 - 0.021267x^2 - 3.29167t^2 - 1.41667E-003T^2 \quad (8)$$

3.2.4. Examining the significance of sentences in the second order model fit indices for initial CO₂ conversion

Table 6 presents the ANOVA results for the second order model fit indices of initial CO₂ conversion. Similar to initial CH₄ conversion, in this design, reaction temperature (T) was the major (F = 4777.95) influencing initial CO₂ conversion, while Co/Ni weight percentage had the slightest impact on response. The ANOVA table shows that since AB and A² recorded p-values greater than 0.05, they are not statistically significant. The p-value (p < 0.0001) shows the high accuracy of the model in predicting initial CO₂ conversion. The predicted R² (0.9370) for the model is properly consistent with the adjusted R² (0.9831). Equations 9 and 10 respectively describe the experimental relationship between the independent variables and initial CO₂ conversion in light of the coded and actual values.

Table (6): ANOVA results for the second order response model for initial CO₂ conversion

Source	Sum of squares	Mean Square	F Value	p-value Prob > F	Coefficient Estimate	Standard Error
Model	5182.18	575.80	91.64	< 0.0001		
A-t	1128.13	1128.13	179.54	< 0.0001	11.88	0.89
B-X	200.00	200.00	31.83	0.0024	-5	0.89
C-T	3003.13	3003.13	477.95	< 0.0001	19.37	0.89
AB	12.25	12.25	1.95	0.2215	-1.75	1.25
AC	324.00	324.00	51.56	0.0008	-9	1.25
BC	90.25	90.25	14.36	0.0128	4.75	1.25
A ²	17.33	17.33	2.76	0.1576	-2.17	1.3
B ²	363.10	363.10	57.79	0.0006	-9.92	1.3
C ²	80.41	80.41	12.80	0.0159	-4.67	1.3

The model based on coded values of the independent variables:

$$X_{CO_2} = + 82.33 + 11.88A - 5.00 B + 19.37C - 1.75A B - 9.00A C + 4.75B C - 2.17A^2 - 9.92B^2 - 4.67 C^2 \quad (9)$$

The model based on actual values of the independent variables:

$$X_{CO_2} = -1443.87500 - 1.0633333x + 154.37500t + 3.35083T - 0.070000x t + 3.80000E-003xT - 0.18000t T - 0.015867x^2 - 2.16667 t^2 - 1.86667E-003T^2 \quad (10)$$

3.2.5. Examining model fitness for H₂:CO molar ratio

Table 7 illustrates the first order model fit indices for the H₂:CO molar ratio. As indicated, temperature and deposition time respectively had the strongest and weakest impact on the H₂:CO molar ratio. Also, the Co/Ni weight percentage had no significant impact on the H₂:CO molar ratio. The small p-value (< 0.0007) shows the fitness of the obtained model for demonstrating the actual relationship between independent variables. Equations 11 and 12 respectively demonstrate the actual and coded values for the predicted models of H₂:CO molar ratio.

Table (7): ANOVA results for the second order response model for H₂:CO molar ratio

Source	Sum of squares	Mean Square	F Value	p-value Prob > F	Coefficient Estimate	Standard Error
Model	0.25	0.085	12.71	0.0007		
A-t	0.05	0.05	7.43	0.0197	0.079	0.029
B-X	1.25E-05	1.25E-05	1.87E-03	0.9663	0.001	0.029
C-T	0.2	0.2	30.69	0.0002	0.160	0.029

The model based on coded values of the independent variables:

$$H_2:CO = + 0.73 + 0.079 A + 1.250E-003B + 0.16C \quad (11)$$

The model based on actual values of the independent variables:

$$H_2:CO = -1.74675 + 5.00000E-005x + 0.078750t + 3.20000E-003T \quad (12)$$

3.2.6. Examining the significance of sentences in the second order model fit indices for catalyst deactivation

Table 8 displays the ANOVA results for the second order model fit indices for catalyst deactivation. Based on the illustrated F-values, temperature (T) had the highest influence on catalyst deactivation (F = 95.22). On the other hand, deposition time (T) had a weaker impact on catalyst deactivation in comparison with Co/Ni ratio (X). Moreover, the small p-value (p < 0.0023) and the proper coefficient of determination (R² is close to 1) suggest the strong correlation between the experimental data and the suggested model. The negligible difference between R² (0.9719) and adjusted R² (0.9213) in the proposed model indicates that the insignificant sentences were removed

from the model. Equations 13 and 14 respectively display the actual and coded values for the predicted models of catalyst deactivation.

Table (8): ANOVA results for the second order response surface model fit indices of catalyst deactivation

Source	Sum of squares	Mean Square	F Value	p-value Prob > F	Coefficient Estimate	Standard Error
Model	53.84	5.98	19.21	0.0023		
A-t	2.42	2.42	7.77	0.0385	-0.55	0.2
B-X	4.2	4.2	13.51	0.0144	0.72	0.2
C-T	29.64	29.64	95.22	0.0002	-1.93	0.2
AB	0.25	0.25	0.8	0.4113	0.25	0.28
AC	2.25	2.25	7.23	0.0434	0.75	0.28
BC	0.09	0.09	0.29	0.6139	-0.15	0.28
A ²	0.043	0.043	0.14	0.7244	0.11	0.29
B ²	14.89	14.89	47.83	0.001	2.01	0.29
C ²	2.56E-04	2.56E-04	8.24E-04	0.9782	8.33E-03	0.29

The model based on coded values of the independent variables:

$$\text{Deactivation: } +3.73 -0.55A + 0.72B -1.92C + 0.25AB + 0.75A C -0.15BC + 0.11A^2 + 2.01B^2 + 8.33E-003C^2 \quad (13)$$

The model based on actual values of the independent variables:

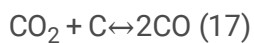
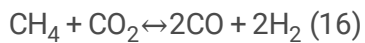
$$\text{Deactivation : } +70.32500 -0.238333x -12.20000t -0.082167T + 1.00000E-002x t -1.20000E-004x T + 0.015000t T + 3.21333E-003x^2 + 0.10833t^2 + 3.33333E-006 T^2 \quad (14)$$

3.3. Examining the impact of different input variables on responses

3.3.1. Impact of input variables on initial CO₂ and CH₄ conversion

The following three-dimensional surface plots (Figs. 7 and 8) illustrate the effect of deposition time (t), Co/Ni weight percentage (X), and reaction temperature (T) on initial CH₄, CO₂ conversion. It is observed that temperature rise led to further initial feed conversion in all the samples (Figs. 7-a, b and 8-a, b). The highest amount of initial CO₂ and CH₄ conversion was recorded when the temperature was 750°C (XCO₂ = 92%, XCH₄ = 97%). This could be attributed to the endothermic nature of DRM. Comparing the results of data analysis in the ANOVA table suggests that temperature is the most determining factor in initial CO₂ and CH₄ conversion. DRM is an endothermic process. Also, previous research shows that increasing temperature leads to measurable rise in the equilibrium constant of main reactions (including DRM and methane decomposition). As a result, better conditions are provided for the

reactions, minimizing the role of the catalyst [21, 39, 40]. Another notable observation is that spinel compounds were not formed, which positively impacts catalytic activity. The results show that, due to the presence of side reactions, especially reverse water gas shift reaction (RWGS) (Eq. 15), the initial ratio of feed conversion is different from DRM stoichiometry standards. More precisely, in all the temperatures, the amount of CO₂ conversion was higher than that of CH₄ (Figs. 7-a and b). On the other hand, given the presence of CO₂ acid gas in DRM, ZrO₂, which is a promoter, can play the role of a catalyst increasing CO₂ conversion through absorbing this gas. In addition, following FESEM analysis, carbon species are more easily available as new base sites through increasing deposition time and reducing particle size. As such, they absorb a greater amount of CO₂ to produce CO, hence increasing the production of synthesis gas (Fig. 8-b and c). This phenomenon not only advances the main reaction (Eq. 16), but also influences reduction in coke formation through reverse Boudouard reaction (Eq. 17) and stability of catalyst performance. Furthermore, because of the presence of more active sites, increasing deposition time leads to higher initial feed conversion. Images (Figs. 7-a, b and 8-a, b) show that the largest amount of feed conversion was recorded for the 4 min deposition time. Studying (Figs. 7-a, b) and (Figs. 8-a, b) also suggests that increasing Co/Ni weight percentage from 25–50% enhances initial feed conversion in DRM. In fact, increasing the portion of the promoter Co heightens Ni activity for decomposing CH₄ and CO₂, leading to the formation of new base sites for further CO₂ absorption. This is in alignment with the findings reported by Zhang et al, who demonstrated that the stability of the bimetallic Co/Ni catalyst goes up if the Co portion increases up to 5% (between 3–5% weight percentage). Increasing Co weight percentage up to 5%, they argued, results in the formation of a larger number of active sites with smaller size and more proper dispersion. In contrast, further rise in the weight percentage of Co/Ni up to 75% relatively reduces catalytic activity since Co covers Ni particles.



3.3.2. Impact of process variables on catalyst deactivation

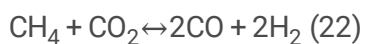
Figure 9 displays three dimensional surface plots for the impact of deposition time (t), Co/Ni weight percentage (X), and reaction temperature (T) on catalyst deactivation. An important factor in catalyst development is its stability under reaction conditions. Carbon deposition and sintering are the main reasons for catalyst deactivation in DRM [6] since carbon is formed through CH₄ decomposition (Eq. 18), the Boudouard reaction (Eq. 19), CO₂ hydrogenation (Eq. 20), and Co hydrogenation (Eq. 21) [40]. From the thermodynamic perspective, methane decomposition is the major factor in coke formation at high temperatures. Nonetheless, the other three reactions are more likely to form coke in lower temperatures. According to Fig. 9 (a and b), increasing reaction temperature leads to reduced catalyst deactivation. It is thus concluded that high temperature blocks three exothermic reactions leading to coke formation. On the other hand, the coke formed at higher temperature can be eliminated through reverse Boudouard reaction [41]. Figure 9 (a and c) also demonstrates that raising deposition time (t) results in declined catalyst deactivation since it leads to reduced Ni particle size and more uniformity and dispersion of the active phase (as observed in the FESEM analysis of catalyst films). In DRM, bigger particle size is more suitable for coke formation reaction [42]. Following GIXRD analysis demonstrated in Fig. 3, increasing Co/Ni weight percentage from 25–50% significantly reduces catalyst deactivation. In fact, according to GIXRD analysis, as particle size reduces, more carbon species are available to react with active CO₂ and produce CO. This

phenomenon is less notable when the particle size goes up. The mechanism of graphite growth is based on the decomposition of hydrocarbons into hydrogen and carbon. In this mechanism, the carbon produced as a result of hydrocarbon decomposition is diffused through metallic particles and is deposited in the form of graphite. The interaction between active Ni phase and Co separates Ni sites from each other, increasing the dispersion of active sites. Materials containing absorbed carbon hardly react with each other, resulting in less coke encapsulation, which improves catalyst stability. Increasing Co/Ni weight percentage up to 75% leads to declined catalyst lifetime, activity, and stability. Partial catalyst deactivation can be attributed to the formation of carbon nanotubes due to a slight increase in particle size.



3.3.3. Impact of process variables on H₂:CO molar ratio

The following figures demonstrate how H₂:CO molar ratio is influenced by different input variables, including deposition time (t), Co/Ni weight percentage (X), and reaction temperature (T). As indicated in Fig. 10 (a and b), increasing the reaction temperature (T) led to higher H₂:CO molar ratio. Raising temperature provides better condition for the main reaction (Eq. 22), which is endothermic, and makes the synthesis gas ratio get closer to the stoichiometric ratio of 1. This can be attributed to the higher strength of DRM compared to that of RWGS reaction (Eq. 23). However, the value is smaller than 1 in all cases, which may be due to RWGS reaction [40, 12, 39]. The scale of RWGS depends on the type of catalyst used in the process. In lower temperatures, it is catalysts' special features that exert a profound influence on their activity. On the other hand, there is a direct relationship between H₂:CO molar ratio and deposition time (t) (Fig. 10-a and c). This could be attributed to the presence of a larger number of small and uniform particles (as observed in FESEM images of catalyst films) which actively participate in CH₄ decomposition. Figures (10-a and c) also shows that Co/Ni weight percentage is not a significant factor in changing H₂:CO ratio. Based on the obtained results, the best synthesis gas ratio (0.96) was recorded when the deposition time was 4 min and the reaction temperature was 750°C.



3.4. Optimizing process variables using RSM

RSM and function maximization technique were exploited in the current study to identify the optimum condition for DRM. Maximum and minimum levels were determined for all the three variables, i.e. deposition time (t), Co/Ni weight percentage (X), and reaction temperature (T), and the maximum and minimum value of the responses were identified. The goal may encompass one of the following options: none, maximum, minimum, target, and in range [43]. The major goal in determining this array of responses was to maximize initial feed conversion and H₂:CO

molar ratio and minimize catalyst deactivation. Table 9 contains the optimization criteria used to assess optimum response values.

Table (9): Optimization criteria for the identified goals to obtain optimum values for responses

Name	Goal	Lower Limit	Upper Limit
deposition time,min	is in range	2	4
Co weight percentage,(w%)	is in range	25%	75%
reaction temperature,°C	is in range	650	750
CH ₄ Conversion, %	maximize	31	92
CO ₂ Conversion, %	maximize	36	97
H ₂ :CO ratio	maximize	0.46	0.96
deactivation, %	minimize	1.6	8.9

3.5. Optimization conditions and validation

Table 10 illustrates 15 solutions offered by Design-Expert. When the solutions are ordered from the best to the worst, solution 1 is selected as the optimum condition for further study. Figure 11 displays response surface of the optimization plot for solution 1. Overall desirability suggests a relatively ideal operation for DRM within the range of the preset condition.

Table (10): Desirability solution

Number	T(°C)	X(%)	t(S)	X _{CH₄}	X _{CO₂}	H ₂ /CO	Deactivation%	Desirability	
1	750	45.04	3.87	95.94	97.86	0.96	1.99335	0.986	Selected
2	750	45.27	3.87	95.94	97.88	0.960007	1.99347	0.986	
3	750	44.56	3.87	95.96	97.82	0.960012	1.99441	0.986	
4	750	45.8	3.87	95.91	97.92	0.960001	1.9949	0.986	
5	749.73	45.49	3.88	95.88	97.88	0.959998	2.00412	0.986	
6	750	44.94	3.85	95.98	97.86	0.95848	1.98697	0.986	
7	750	45.91	3.84	95.93	97.94	0.958332	1.9881	0.986	
8	750	44.56	3.97	95.75	97.74	0.968143	2.03003	0.985	
9	750	43.76	3.82	96.02	97.74	0.95606	1.9831	0.985	
10	750	45.61	3.99	95.65	97.80	0.969704	2.0382	0.985	
11	750	47.63	3.35	95.87	97.77	0.919237	1.85448	0.97	
12	746.88	34.6	4	93.77	95.31	0.960005	2.44518	0.963	
13	750	47.29	2.77	93.95	96.12	0.873574	1.74365	0.946	
14	750	49.8	2.71	93.56	96.02	0.869246	1.76412	0.942	
15	750	43.85	2.54	92.19	94.52	0.85544	1.75593	0.928	

3.6. Evaluation of time on stream in microchannel reactor at optimum condition

The stability tests were carried out under optimum condition, i.e. the sample was under the pressure of 1 atm; the temperature was set at 750°C; the feed contained CH₄, CO₂, and helium with a molar ratio of 1:1:8; the flow rate was 10 mL/min; residence time was 3.12 s; 13.04 mg of catalyst was used; and a space velocity of 46000 mL.g⁻¹.h⁻¹ was applied. Sampling was done every hour during the test. According to Fig. 12, the percentage of initial CH₄ conversion, the percentage of initial CO₂ conversion, and H₂:CO molar ratio were relatively stable during 28 hours. Besides, carbon balance was measured to assess weight loss caused by carbon deposition in the sample. The carbon balance was

between 92% and 96% during the experiment, which shows that CH₄ and CO₂ were almost fully converted to CO. The amount of carbon deposition on catalyst surface is negligible and is caused by carbon formation during CH₄ decomposition. Carbon deposition on the catalyst pellet may be attributed to limitation in mass and heat transfer. This limitation leads to the formation of hot spots and local rich carbon species on some active sites within the pores of the catalyst. However, when the catalysts are applied as a thin film, the active surface is in contact with a thin layer. Since no porous structure is formed in this condition, there is no significant accumulation of local heat and mass.

4. Conclusion

This study investigated synthesis gas production through DRM using a microchannel reactor and PVD for catalyst coating. ANOVA was also exploited to explore the impact of the process on initial feed conversion, catalyst deactivation, and H₂:CO molar ratio. RSM was further utilized to identify the optimum condition and examine the interaction between independent variables (including coating time, Co/Ni weight percentage, and reaction time) and their impact on responses. The results suggest that using PVD can offer a simple way to obtain a uniform structure of active phase with proper dispersion. The major advantages of using PVD for catalyst coating are the ability to control the coating rate from one nanometer to several micrometers, high speed of the coating process, negligible surface damages in the produced coating, high coating purity given that the process is accomplished in vacuum, and higher capability to control microstructures and coating morphology in comparison with other methods. Comparing the performance of the fixed-bed reactor used by Haghghi et al. (under these conditions: total flow rate of 40 ml/min; 100 mg of catalyst; Co weight percentage of 3%; T = 850; and GHSV = 24000 mL.g⁻¹.h⁻¹) and that of the microchannel reactor used in the current study (under these conditions: total flow rate of 10 ml/min; 13.04 mg of catalyst; Co/Ni weight percentage of 45.01%; T = 750; and GHSV = 46000 mL.g⁻¹.h⁻¹) shows that microchannel reactor is a suitable replacement for fixed-bed reactor because the former relatively increases initial feed conversion and space velocity and reduces catalyst consumption (approximately 87%). Moreover, the results of the stability test at the optimum condition (i.e., the sample was under the pressure of 1 atm; the temperature was set at 750°C; the feed contained CH₄, CO₂, and helium with a molar ratio of 1:1:8; the flow rate was 10 mL/min; residence time was 3.12 s; 13.04 mg of catalyst was used; and a space velocity of 46000 mL.g⁻¹.h⁻¹) shows that the percentage of initial CH₄ conversion, the percentage of initial CO₂ conversion, and H₂:CO molar ratio were relatively stable during 28 hours. This shows a proper level of activity and stability stemming from improved mass and heat transfer during the stream. The findings suggest that if appropriate methods are used for catalyst synthesis and optimum amount of promoter is identified, microchannel reactors can be implemented using a significantly smaller amount of catalyst and lower operation temperature to yield better efficiency and stability and lower costs compared to other methods.

References

1. K. Li, H. Wang, Y. Wei, D. Yan, International Journal of hydrogen energy 36 (2011) 3471-3482.
2. P. Estifae, M. Haghghi, A.A. Babaluo, N. Rahemi, M. Fallah Jafari, The Beneficial Use of Non-thermal Plasma in Synthesis of Ni/Al₂O₃-MgO Nanocatalyst Used in Hydrogen Production from Reforming of CH₄/CO₂ Greenhouse Gases, Journal of Power Sources, 257 (2014) 364-373.
3. J. Ma, N. Sun, X. Zhang, N. Zhao, F. Xiao, W. Wei, Y. Sun, Catalysis Today 148(2009)221-231.
4. J.R. Rostrup-Nielsen, Catalysis today 63 (2000) 159-164
5. A.P. York, T. Xiao, M.L. Green, Topics in Catalysis 22(2003)345-358.
6. M. Usman, W.W. Daud, H.F. Abbas, Renewable and Sustainable Energy Reviews 45 (2015) 710-744.
7. Z. Hou, P. Chen, H. Fang, X. Zheng, T. Yashima, International journal of hydrogen energy 31 (2006) 555-561.
8. L. Zhang, Q. Zhang, Y. Liu, Y. Zhang, Dry reforming of methane over Ni/Mgo-Al₂O₃, catalysts prepared by two-step hydrothermal method, Appl. Surf. Sci. 389 (2016) 25-33.
9. N.A. Pechimuthu, K.K. Pant, S.C. Dhingra, Deactivation Studies over Ni-K/CeO₂-Al₂O₃ Catalyst for Dry Reforming of Methane, Industrial & Engineering Chemistry Research, 46 (2007) 1731-1736

10. V.Y. Bychkov, Y.P. Tyulenin, AA Firsova, EA Shafranovsky, AY Gorenberg. V.N. Korchak. Carbonization of nickel catalysts and its effect on methane dry reforming, *Appl. Catal. A* 453 (2013) 71-79.
11. N. Rahemi, M. Haghighi, AA Babaluo, M.F. Jafari. S. Khorram, Conversion of CH₄/CO₂ to syngas over Ni-Co/Al₂O₃-ZrO₂, nanocatalyst synthesized via plasma assisted Co-impregnation method: surface properties and catalytic performance, *J. Appl. Phys.* 114 (2013) 0943071-09430110.
12. Sajjadi, S.M., Haghighi, M., Alizadeh Eslami, A., Rahmani, F., 2013. Hydrogen production via CO₂-reforming of methane over Cu and Co doped Ni/Al₂O₃ nanocatalyst: impregnation vs. sol-gel method and effect of process conditions and promoter. *J. Sol-Gel Sci. Technol.* 67, 601-617
13. R Martinez, E. Romero, C. Guimon, R. Bilbao, CO₂ reforming of methane over coprecipitated Ni-Al catalysts modified with lanthanum, *Appl. Catal. A* 274 (2004) 139-149.
14. K. Jabbour, P. Massiani. A. Davidson, S. Casale, N. El Hassan, Ordered mesoporous "one-pot* synthesized Ni-Mg(Ca)- Al₂O₃ as effective and remarkably stable catalysts for combined steam and dry reforming of methane (CSDRM), *Appl. Catal. B* 201 (2017) 527-542.
15. D.Li, R. Li, M. Lu. X. Lin. Y. Zhan, L Jiang, Carbon dioxide reforming of methane over Ru catalysts supported on Mg-Al oxides: a highly dispersed and stable Ru/Mg(Al)O catalyst, *Appl. Catal B* 200 (2017) 565-577.
16. S.M. Sajjadi, M. Haghighi, F. Rahmani, Dry reforming of greenhouse gases CH₄/ CO₂, over MgO-promoted Ni-Co/Al₂O₃-ZrO₂ nanocatalyst: effect of MgO addition via sol-gel method on catalytic properties and hydrogen yield. *J.Sol-Gel. Sci. Technol.* 70 (2014) 111-124.
17. J.H. Song, S.J. Han, J. Yoo, S. Park, D.H. Kim, I.K. Song, Effect of Sr content on hydrogen production by steam reforming of ethanol over Ni-Sr/Al₂O₃-ZrO₂ xerogel catalysts, *Journal of Molecular Catalysis A: Chemical*, 418–419(2016)68-77.
18. R.K. Singha, A. Shukla, A. Yadav, S. Adak, Z. Iqbal, N. Siddiqui, R. Bal, Energy efficient methane tri-reforming for synthesis gas production over highly coke resistant nanocrystalline Ni–ZrO₂ catalyst, *Applied Energy*, 178 (2016) 110-125.
19. M. Rezaei, S.M. Alavi, S. Sahebdehfar, P. Bai, X. Liu, Z.-F. Yan, CO₂ reforming of CH₄ over nanocrystalline zirconia-supported nickel catalysts, *Applied Catalysis B:Environmental*, 77 (2008) 346-354.
 [20] D. San-José-Alonso, J. Juan-Juan, M.J. Illán-Gómez, M.C. Román-Martínez, Ni, Co and bimetallic Ni-Co catalysts for the dry reforming of methane, *Applied Catalysis A:General*, 371 (2009)54-59.
 [21] J. Zhang, H. Wang, A.K. Dalai, Development of stable bimetallic catalysts for carbon dioxide reforming of methane, *Journal of Catalysis*, 249 (2007) 300-310.
20. S.Therdthianwong, C.Siangchin, A.Therdthianwong, Improvement of coke resistance of Ni/Al₂O₃ catalyst in CH₄/CO₂reforming by ZrO₂ addition. *Fuel Process. Technol.* 2008, 89, 160–168.
21. .Rahemi, N., Haghighi, M., Babaluo, A.A., Fallah Jafari, M., Estifaeae, P., 2013. Synthesis and physicochemical characterizations of Ni/Al₂O₃-ZrO₂ nanocatalyst prepared via impregnation method and treated with non-thermal plasma for CO₂ reforming of CH₄. *J. Ind. Eng. Chem.* 19, 1566-1576.
22. Mahboob, s; Haghighi, M, Rahmani, F.Sonochemically pereparation and characterization of bimetallic Ni-Co/Al₂O₃–ZrO₂ nanocatalyst *Ultrasonics Sonochemistry* (2017), 38-49
23. Sharifi, M.; Haghighi, M.; Rahmani, F.; Karimipour, S. Syngas production via dry reforming of CH₄ over Co-and Cu-Promoted Ni/Al₂O₃–ZrO₂ nanocatalysts synthesized via sequential impregnation and sol-gel methods. *J. Nat. Gas Sci. Eng.* 2014, 21, 993–1004.

24. O. Laguna, M. Dominguez, M. Centeno, J. Odriozola, *New Materials for Catalytic Applications* (2016) 81-120.
25. T. Hou, S. Zhang, T Xu, W. Cai, *Chemical Engineering Journal* 255 (2014)149-155
26. D.H. Kim, S.H. Kim, J.Y. Byun, *Chemical Engineering Journal* 280 (2015) 468-474.
27. Sangsong, S.; et al. Dry Methane Reforming Performance of Ni-based Catalyst Coated onto Stainless Steel Substrate. *Energy Procedia* 2015, 79, 137–142.
28. M. Mahmoudizadeh, A. Irankhah, R. Trankhah, M. Jafari, *Chemical Engineering & Technology* 39 (2016) 322-330.
29. [31] Bawornruttanaboonya, K.; et al. Comparative evaluation of autothermal reforming of biogas into synthesis gas over bimetallic Ni-Re/AL₂O₃ catalyst in fixed-bed and coated-wall microreactors: A
30. computational study. *Int. J. Hydrogen Energy* 2018, 43, 13237.
31. Rezaei, R.; Moradi, G. Study of the performance of dry methane reforming in a microchannel reactor using sputtered Ni/Al₂O₃ coating on stainless steel. *Int. J. Hydrogen Energy* 2018, 43,
32. -21385.
33. O. Sanz, F. Echave, F. Romero-Sarria, J. Odriozola, M. Montes, *Renewable Hydrogen Technologies: Production, Purification, Storage, Applications and Safety* (2013) 201-224.
34. J.E. Mahan. *Physical Vapor Deposition of Thin Films*, by John E. Mahan 336 (2000) .
35. S. Geng, Y. Li, Z. Ma, S. Zhu, F. Wang, *Journal of Power Sources* 232 (2013) 66-73.
36. S. Geng, Q. Wang, W. Wang, S. Zhu, F. Wang, *international journal of hydrogen energy* 37(2012)916-920.
37. S. Geng. Q. Zhao, Y. Li, J. Mu, G. Chen, F. Wang, S. Zhu, *International journal of hydrogen energy* 42 (2017) 10298-10307 .
38. Forutan, H.; et al. Expert representation chemical looping reforming: A comparative study of Fe, Mn, Co and Cu as oxygen carriers supported on Al₂O₃. *J. Ind. Eng. Chem.* 2015, 21, 900–911.
39. M. Haghghi, Z.q.Sun, J. h Wu , J. Bromly, H. L.We, E.Ng, Y.Wang, D. k Zhang, "On the reaction mechanism of CO₂ reforming of methane over a bed of coal char," *Proceedings of the Combustion Institute*, Vol. 31, No. 2, pp. 1983-1990,2007.
40. MK. Nikoo, N. Amin. *Fuel Processing Technology* 92 (2011) 678-691.
41. Chen, Q.; et al. Temperature-dependent anti-coking behaviors of highly stable Ni-CaO-ZrO₂ nanocomposite catalysts for CO₂ reforming of methane. *Chem. Eng. J.* 2017, 320, 63–73.
42. S.J.H. Rad, M. Haghghi, A.A. Eslami.F. Rahmani, N. Rahemi *International Journal of Hydrogen Energy* 41 (2016) 5335- 5350.
43. G. Derringer, R. Suich, *Journal of quality technology* 12 (1980) 214-219.

Figures

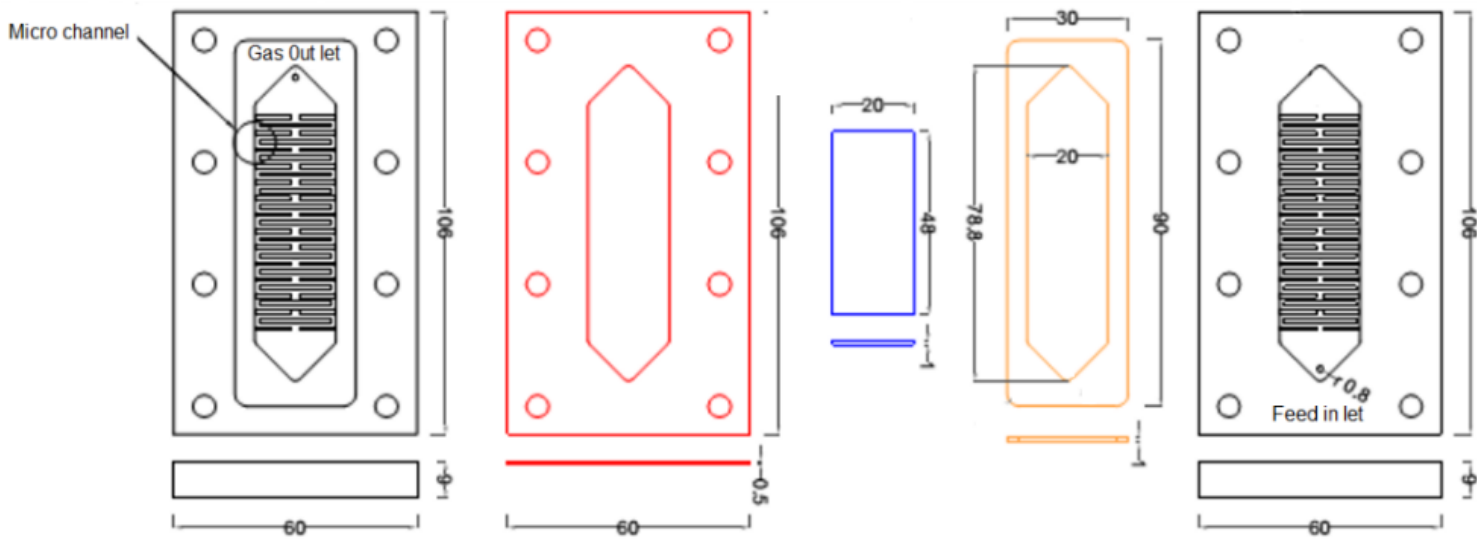


Figure 1

A schematic representation of the microreactor used in the current study

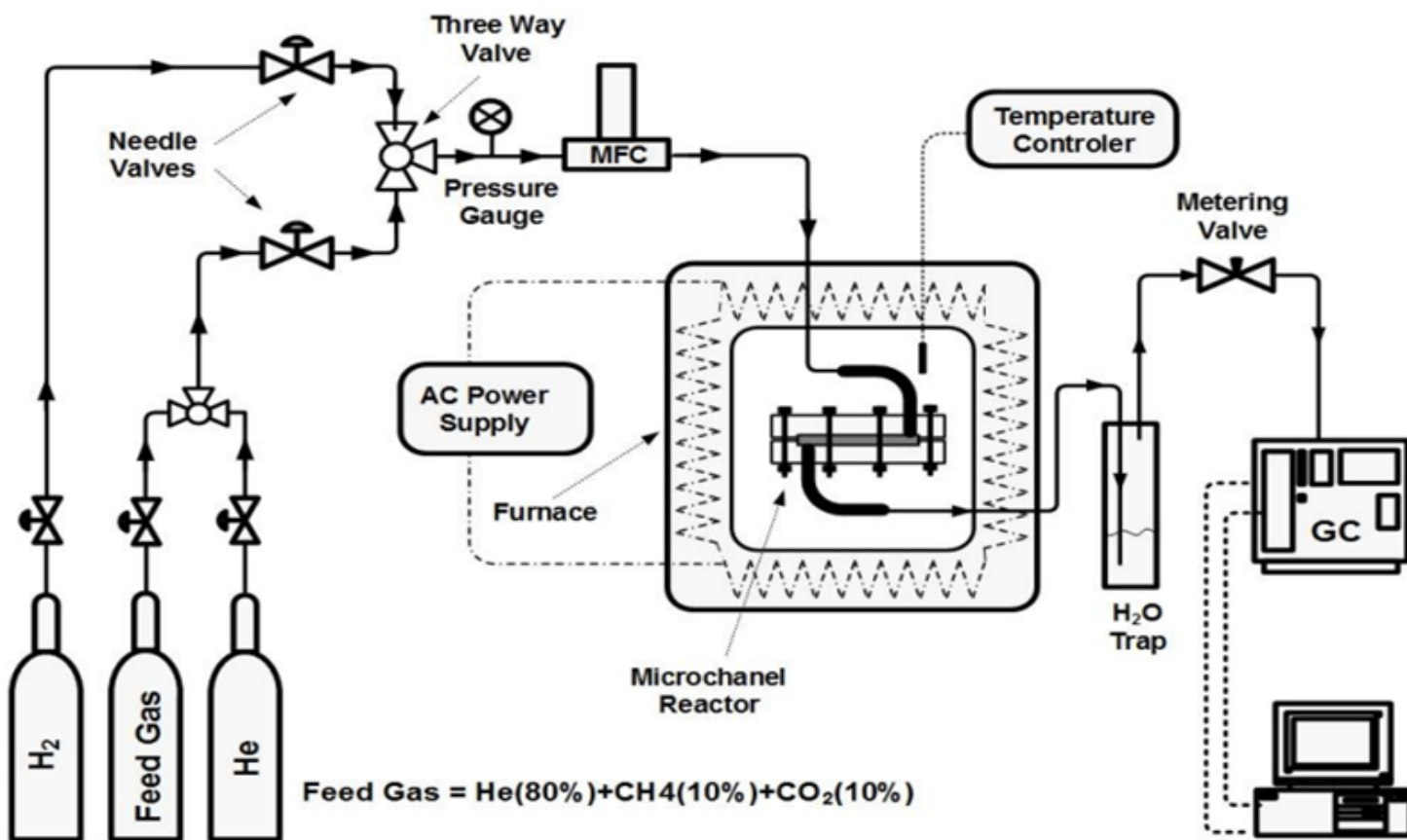


Figure 2

A schematic representation of the experimental system used for producing synthesis gas in DRM

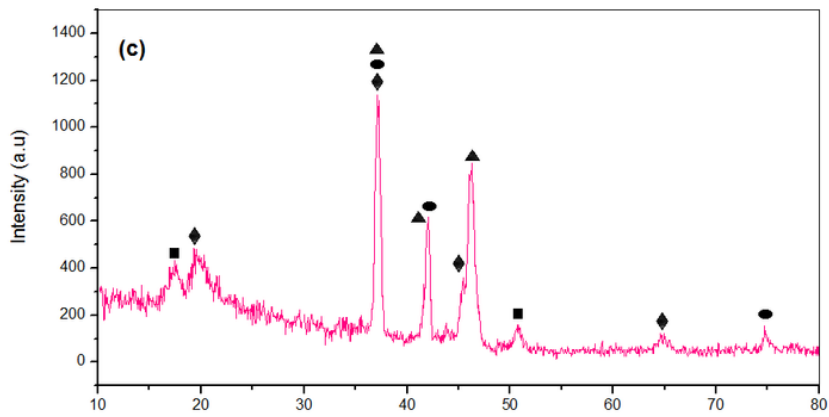
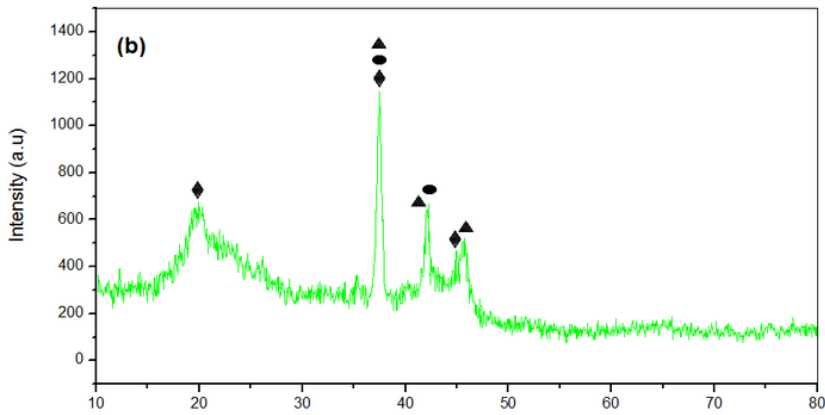
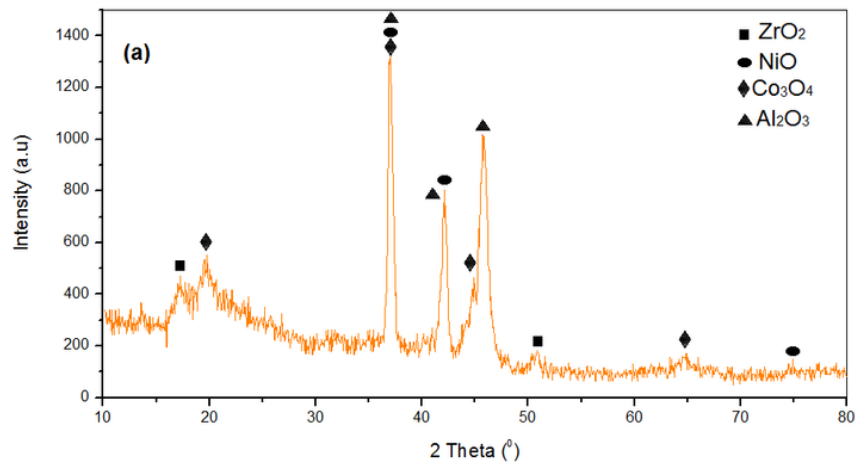
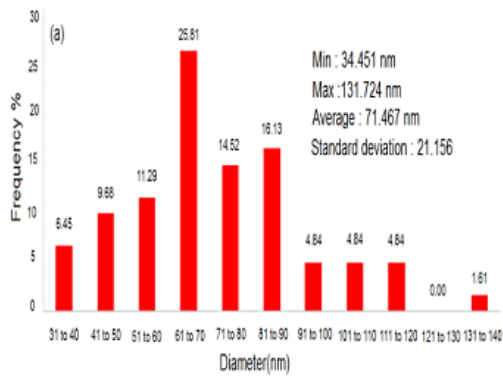
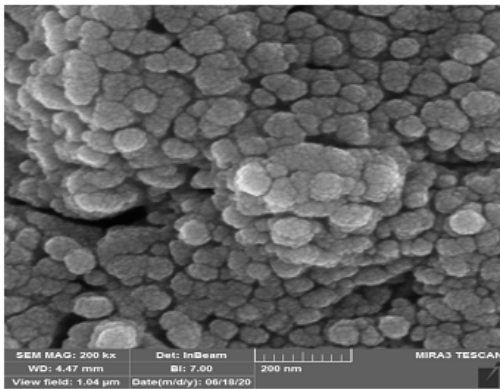
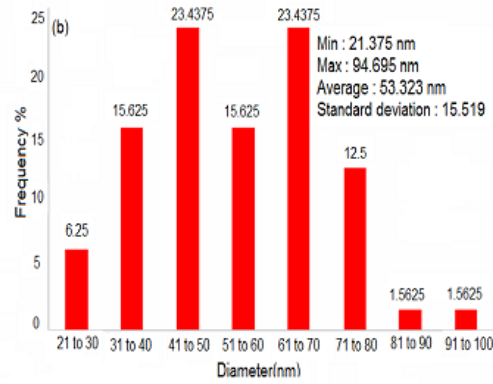
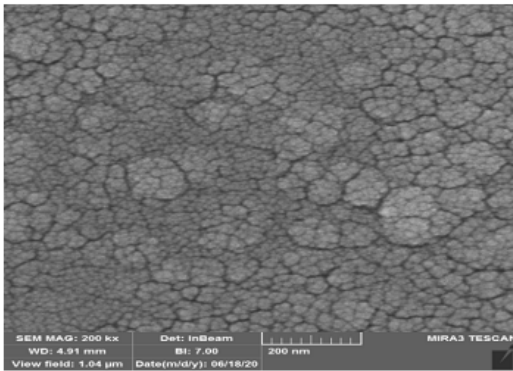


Figure 3

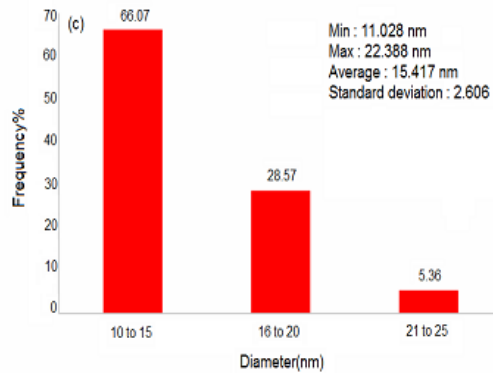
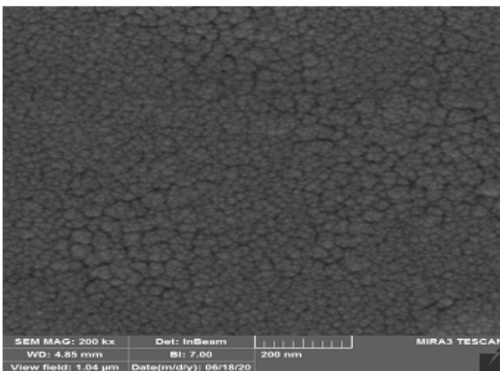
The results of GIXRD for the Ni-Co/Al₂O₃-ZrO₂ catalytic films with various Co/Ni weight percentages (a = 25%, b = 50%, and c = 75%) at 4 min deposition time.



(t=2min)



(t=3min)



(t=4min)

Figure 4

FESEM-surface images of Ni-Co/Al₂O₃-ZrO₂ catalyst coatings at 2, 3, and 4 min deposition times with Co/Ni weight percentage of 50% magnified on scale of 200 nm

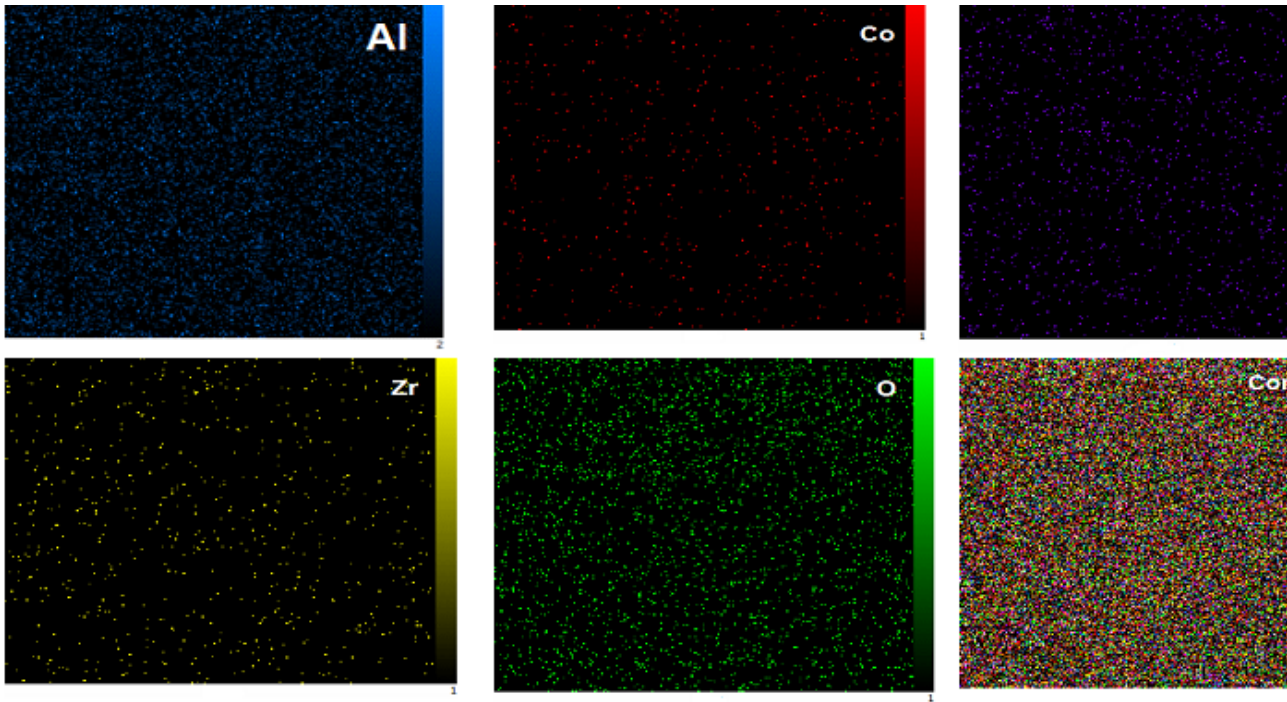


Figure 5

EDX dot-mapping analysis of Ni-Co/ Al_2O_3 - ZrO_2 catalyst coatings at the 4 min deposition time and Co/Ni weight percentage of 50%

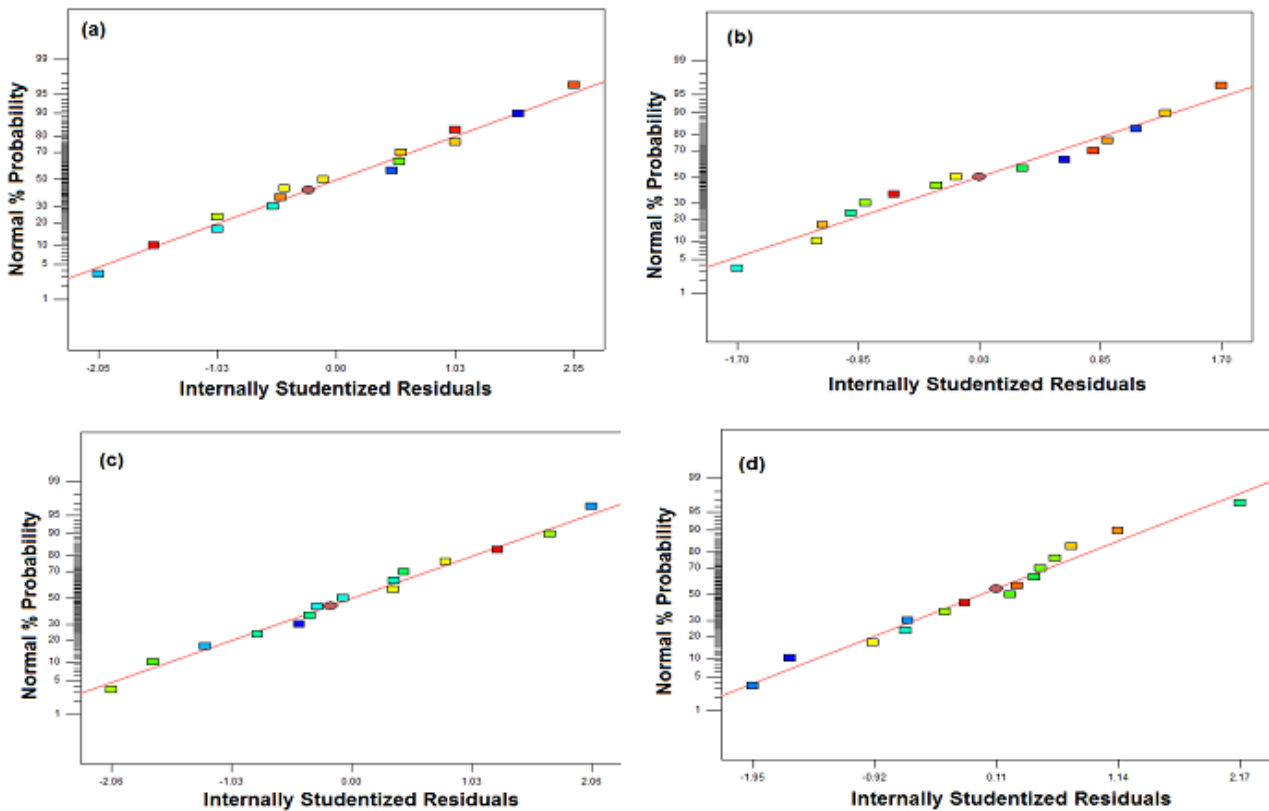


Figure 6

Normal probability plot of studentized residuals for initial conversion of CH₄ (a) and CO₂ (b), catalyst deactivation (c), and H₂/CO molar ratio (d)

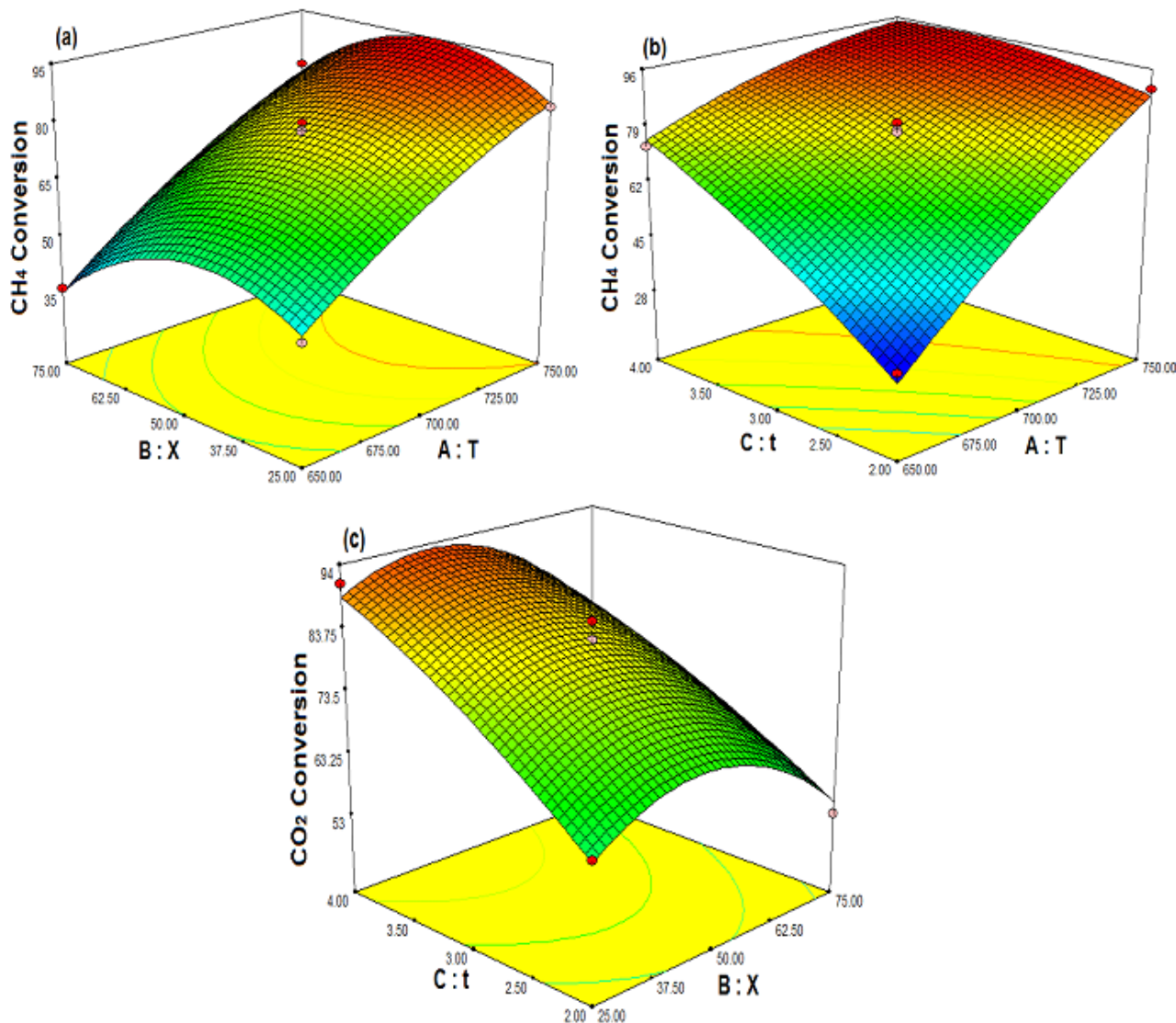


Figure 7

Three dimensional surface plots for the predicted model of initial CH₄ and CO₂ conversion as a function of (a) reaction temperature (T) and Co/Ni weight percentage (X) at 3 min deposition time; (b) deposition time (t) and reaction temperature (T) at the Co/Ni weight percentage of 50%; (C) Co/Ni weight percentage (X) and reaction temperature (t) at 700 °C reaction temperature.

Figure 8

Three dimensional surface plots for the predicted model of initial CH₄ and CO₂ conversion as a function of (a) reaction temperature (T) and Co/Ni weight percentage (X) at 3 min deposition time; (b) deposition time (t) and reaction temperature (T) at the Co/Ni weight percentage of 50%; (C) Co/Ni weight percentage (X) and reaction temperature (t) at 700 °C reaction temperature.

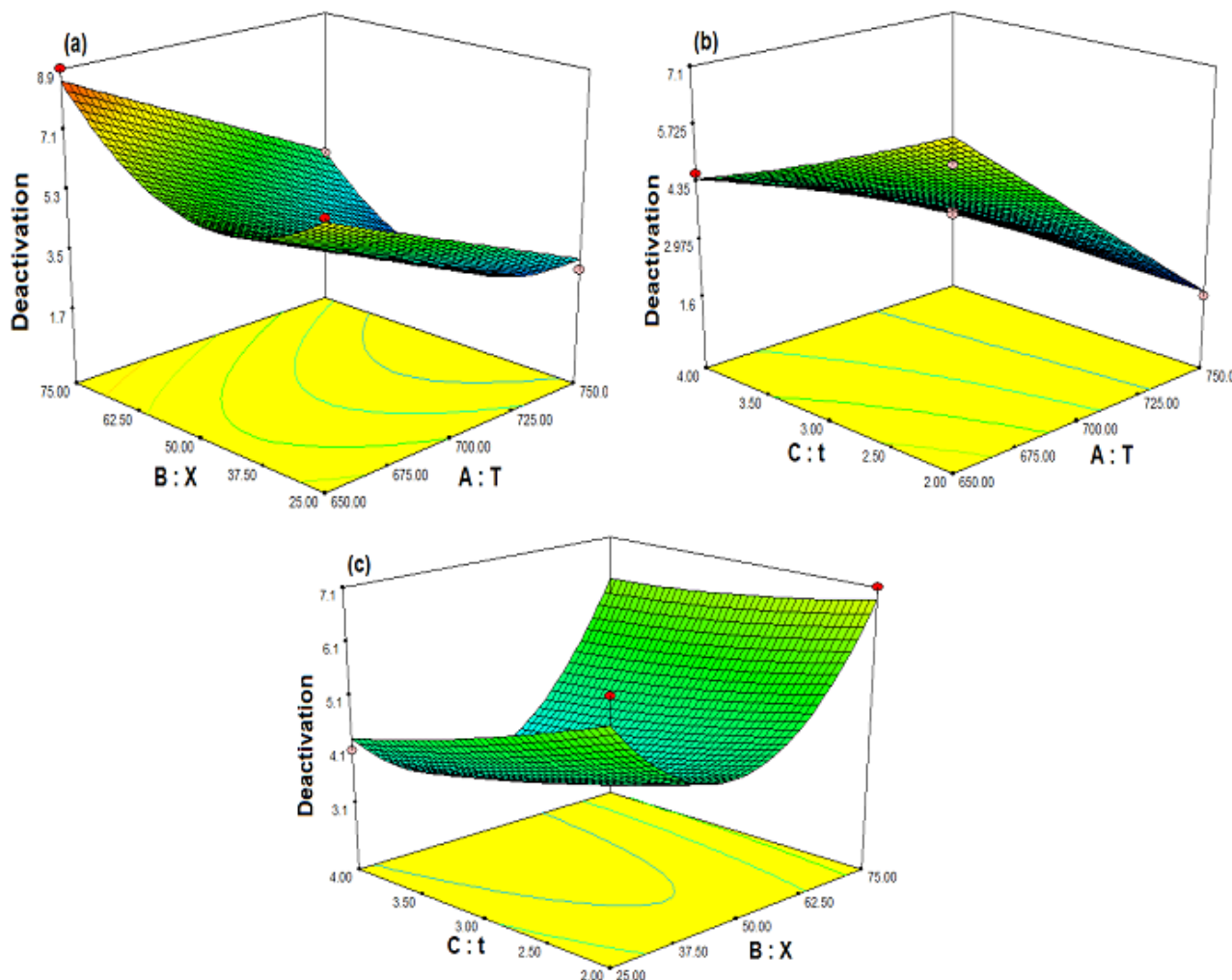


Figure 9

Three dimensional surface plots for the predicted model of catalyst deactivation as a function of (a) Co/Ni weight percentage (X) and reaction temperature (T) at 3 min deposition time (b) deposition time (t) and reaction temperature (T) at the Co/Ni weight percentage of 50%; (C) deposition time (t) and Co/Ni weight percentage (X) at 700 °C reaction temperature.

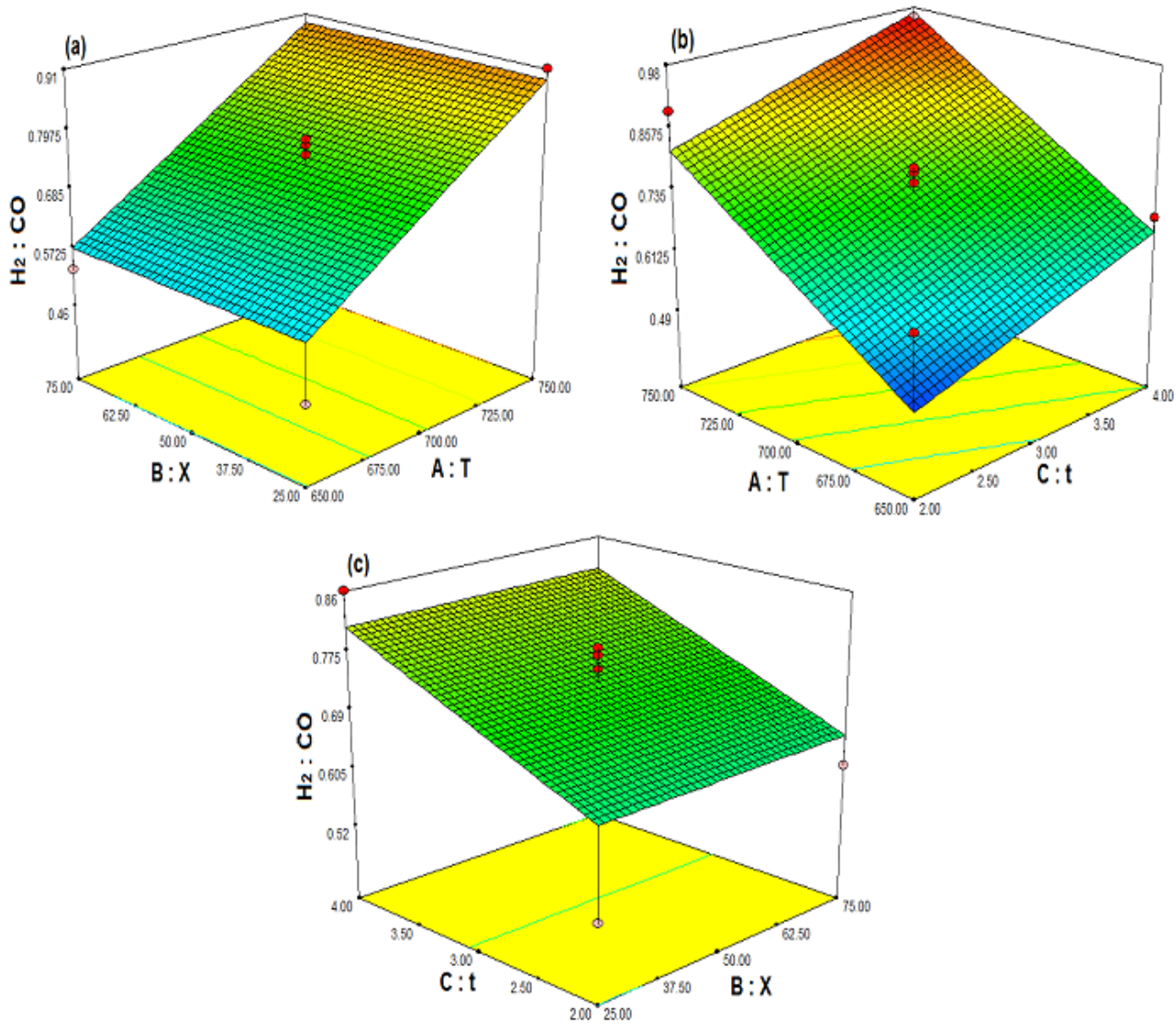


Figure 10

Three dimensional surface plots for the predicted model of $H_2:CO$ molar ratio as a function of (a) Co/Ni weight percentage (X) and reaction temperature (T) at 3 min deposition time (b) deposition time (t) and reaction temperature (T) at the Co/Ni weight percentage of 50%; (c) deposition time (t) and Co/Ni weight percentage (X) at 700 °C reaction temperature.

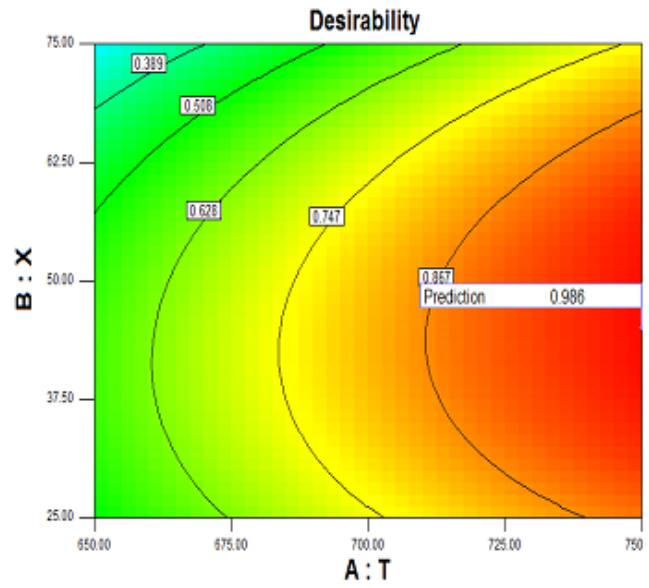
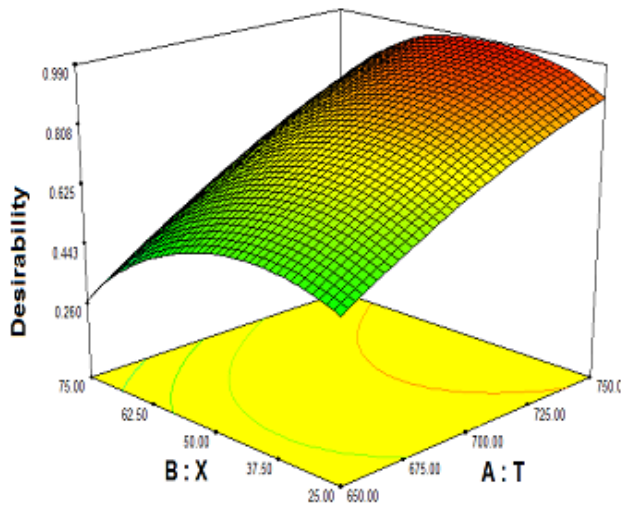


Figure 11

Response surface of the optimization plot for solution 1

Figure 12

Stability results under the optimum condition